JGR Oceans

RESEARCH ARTICLE
10.1029/2024JC021127

Model Biases in Simulating Extreme Sea Ice Loss Associated With the Record January 2022 Arctic Cyclone

Edward Blanchard-Wrigglesworth[1], Samuel Brenner[2], Melinda Webster[3], Chris Horvat[2], Øyvind Foss[4], and Cecilia M. Bitz[1]

[1]Department of Atmospheric Sciences, University of Washington, Seattle, WA, USA, [2]Brown University, Providence, RI, USA, [3]Applied Physics Lab, University of Washington, Seattle, WA, USA, [4]Norwegian Polar Institute, Tromsø, Norway

Abstract In January 2022, the strongest Arctic cyclone on record resulted in a record weekly loss in sea ice cover in the Barents-Kara-Laptev seas. While ECMWF operational forecasts skillfully predicted the cyclone, the loss in sea ice was poorly predicted. We explore the ocean's response to the cyclone using observations from an Argo float that was profiling in the region, and investigate model biases in simulating the observed sea ice loss in a fully coupled GCM. The observations showed changes over the whole ocean column in the Barents Sea after the passage of the storm, cooling and mixing with enough implied heat release to melt roughly 1 m of sea ice. We replicate the observed cyclone in the GCM by nudging the model's winds to observations above the boundary layer. In these simulations, the associated loss of sea ice is only about 10%–15% of the observed loss, and the ocean exhibits very small changes in response to the cyclone. With the use of a simple 1-D ice-ocean model, we find that the overly strong ocean stratification in the GCM may be a significant source of model bias in its simulated response to the cyclone. However, even initialized with observed stratification profiles, the 1-D model also underestimated mixing and sea ice melt relative to the observations.

Plain Language Summary Extreme storms in the Arctic can significantly impact the ocean and sea ice state. In January 2022, the strongest Arctic storm on record resulted in a record loss of sea ice. The storm was well predicted by the ECMWF operational forecasts, yet the loss of sea ice was not. Here we further study the impact that the storm had on the ocean, and how well a fully coupled global climate model simulates the observed response in sea ice and ocean to the storm. We do this by nudging the winds in the model to observations. In observations, the ocean responded to the storm by cooling and mixing to full depth in the Barents Sea, releasing enough heat to melt a significant amount of sea ice. In contrast, the model's simulated sea ice and ocean response to the storm is much smaller than estimated in observations. The model's ocean stratification prior to the storm is significantly stronger than observed and is likely a source of bias, which we confirm with the use of a simple one dimensional model.

Edward Blanchard-Wrigglesworth and Samuel Brenner contributed equally to this work.

Key Points:

- An Argo float showed cooling and mixing in the Barents Sea during a record Arctic cyclone, accounting for the associated record sea ice loss
- A coupled GCM with winds nudged to observations shows much smaller changes in sea ice and ocean structure with the passage of the cyclone
- A 1-D ocean model shows that too-strong stratification in the GCM is a main source of bias in its sea ice and ocean response to the cyclone

Supporting Information:

Supporting Information may be found in the online version of this article.

Correspondence to:

E. Blanchard-Wrigglesworth, edwardbw@uw.edu

Citation:

Blanchard-Wrigglesworth, E., Brenner, S., Webster, M., Horvat, C., Foss, Ø., & Bitz, C. M. (2024). Model biases in simulating extreme sea ice loss associated with the record January 2022 Arctic cyclone. *Journal of Geophysical Research: Oceans*, *129*, e2024JC021127. https://doi.org/10.1029/2024JC021127

Received 18 MAR 2024
Accepted 20 AUG 2024

Author Contributions:

Conceptualization: Edward Blanchard-Wrigglesworth, Samuel Brenner, Melinda Webster, Chris Horvat, Cecilia M. Bitz
Data curation: Øyvind Foss
Formal analysis: Edward Blanchard-Wrigglesworth, Samuel Brenner
Funding acquisition: Melinda Webster, Chris Horvat, Cecilia M. Bitz
Investigation: Edward Blanchard-Wrigglesworth, Samuel Brenner
Methodology: Edward Blanchard-Wrigglesworth, Samuel Brenner, Melinda Webster, Chris Horvat, Cecilia M. Bitz

1. Introduction

Arctic cyclones play a significant role in driving sea ice variability (e.g., Blanchard-Wrigglesworth, Donohoe, et al., 2021; Clancy et al., 2022; Wang et al., 2020; Zhang et al., 2013). Arctic cyclones can also impact waves (e.g., Waseda et al., 2021), which can themselves break up sea ice (e.g., Asplin et al., 2012; Marko, 2003; Stopa et al., 2016), and enhance vertical ocean mixing — potentially leading to sea ice loss through enhanced ocean-ice heat flux and basal sea ice melt (e.g., Meyer et al., 2017; Smith et al., 2018). In January 2022, an extreme Arctic cyclone developed over East Greenland and traveled northeastward across the Barents and Kara Seas into the Arctic. The cyclone reached its peak intensity on 24 January 2022 over the marginal sea ice zone east of Svalbard, and its central pressure of 932 mb was the lowest on record (for any calendar month) since 1979 north of 70°N as estimated in the ERA5 reanalysis (Blanchard-Wrigglesworth et al., 2022). The cyclone produced extreme surface winds (>100 km/hr) and large (>8 m) ocean waves in the Barents Sea that impinged upon the sea ice and traveled over 100 km into the ice-pack. It resulted in a record weekly loss in sea ice area (SIA) of almost 0.5 million km^2 in the Barents-Kara-West Laptev seas between January 21 and January 27; the loss was over 30% larger than the previous record SIA weekly loss since 1979. Operational forecasts from the high-resolution state-of-the-art ECMWF IFS model showed high skill in forecasting the cyclone in the week leading to the event, yet the forecasts' skill in simulating the observed sea ice loss was poorer, forecasting only about 40%–50% of the observed SIA loss. Satellite and reanalysis-derived estimates of the surface energy budget during the cyclone showed limited energy fluxes from the atmosphere into the surface, implying that atmospheric heat only

Project administration: Melinda Webster, Chris Horvat, Cecilia M. Bitz
Software: Edward Blanchard-Wrigglesworth, Samuel Brenner
Supervision: Edward Blanchard-Wrigglesworth, Melinda Webster, Chris Horvat, Cecilia M. Bitz
Validation: Edward Blanchard-Wrigglesworth, Samuel Brenner, Øyvind Foss
Writing – original draft: Edward Blanchard-Wrigglesworth, Samuel Brenner
Writing – review & editing: Edward Blanchard-Wrigglesworth, Samuel Brenner, Melinda Webster, Chris Horvat, Øyvind Foss, Cecilia M. Bitz

accounted for limited sea ice melt and that significant sea ice loss must have resulted from enhanced ocean heat fluxes to the sea ice.

The Barents Sea has seen considerable change in recent decades (e.g., Gerland et al., 2023), experiencing an increased flux of warm, saline Atlantic water (Årthun et al., 2012) as part of a process referred to as "Atlantification" of the Arctic (Polyakov et al., 2017), and an associated significant loss of sea ice (Onarheim & Årthun, 2017). Ocean stratification in the northern, ice-covered sectors has weakened (Lind et al., 2018), and surface air temperatures have experienced the fastest rate of warming in recent decades globally, with annual-mean temperature trends of up to 1°C per decade over 1979–2021 (Rantanen et al., 2022). Yet, global climate models (GCMs) struggle to simulate the observed sea ice decline in this region (D. Li et al., 2017), even with their atmospheric circulation nudged to observations (Roach & Blanchard-Wrigglesworth, 2022). GCMs also show a large spread in the simulated ocean water volume and heat transport into the Barents Sea (Dörr et al., 2024; Ilıcak et al., 2016), a too-deep warm Atlantic Water layer (Ilıcak et al., 2016), and ocean stratification inconsistent with observations (Dörr et al., 2024), representing a key challenge to modeling of the present and future Arctic Ocean (Allende et al., 2023; Khosravi et al., 2022; Muilwijk et al., 2023). In the Barents Sea and the Eurasian Basin of the Arctic Ocean, the AW layer is generally located relatively close to the surface, below a sea ice-influenced fresh and cold surface layer. Previous observations from the area (Meyer et al., 2017; Peterson et al., 2017) show that storms can efficiently bring ocean heat toward the surface during winter sea ice-covered conditions, causing basal sea-ice melt rates of up to 25 cm/day. Subsequent melt of sea ice from below contributes to the strong and lasting impact of storms on sea ice cover in the area (Graham et al., 2019; Itkin et al., 2017).

In this work, we present evidence linking ocean heat changes to sea ice loss during the January 2022 cyclone by examining observed ocean properties obtained from an Argo float in the Barents Sea during the cyclone. We then test the fidelity of a widely used GCM, the NCAR CESM1-CAM5 model (Gent et al., 2011), in replicating the observed response of the sea ice and ocean to the cyclone by nudging the model's winds to the observed winds from January 2022. GCMs are widely used tools to project future changes in climate and sea ice cover and are increasingly being used for short-term sea ice forecasting (E. Hunke et al., 2020). Recent modeling experiments that nudge model winds to the observed circulation have shown great promise as a methodology to understand long-term trends and interannual variability of SIA (Blanchard-Wrigglesworth, Roach, et al., 2021; Roach & Blanchard-Wrigglesworth, 2022), and directly evaluate GCMs with in situ Arctic observations (Pithan et al., 2022). At the same time, it is known that free-running CMIP GCMs have biased damped Arctic sea ice variability at weather timescales (Blanchard-Wrigglesworth, Donohoe, et al., 2021), the reasons for which are unclear. Thus, testing how a widely-used GCM simulates a single observed extreme event of sea ice variability at weather timescales that is strongly related to an observed atmospheric event may provide insight into model biases in the simulation of sea ice variability and atmosphere/sea ice coupling and offer paths forward for future model development.

We also investigate the impact of climate mean state and ice-floe size on model biases and in simulated sea ice loss sensitivity to the cyclone. To do this, we run different sets of experiments across a range of 21st-century mean states, and with different ice floe-size values. While fully coupled wave-ice ocean modeling in the GCM is still in development, a change to smaller floe-size values allows us to partly test the hypothesis that ocean waves may have played an important role in explaining the forecast biases in the sea ice forecasts (Blanchard-Wrigglesworth et al., 2022). However, we note that in the CESM sea ice component, the sea ice momentum equation terms are not related to the floe size distribution, so these smaller floe size experiments only impact thermodynamic (lateral melt) processes.

Finally, to gain further understanding of the role of ocean stratification in sea ice and heat flux changes, we run a series of experiments with a one-dimensional ocean mixing model coupled to a thermodynamic sea ice model. By initializing the model with temperature and salinity profiles corresponding to either the Argo float observations before the cyclone or to corresponding profiles extracted from the CESM simulation, we isolate the impact of the ocean's vertical structure on the observed changes in sea ice and heat flux. These experiments provide context for sea ice changes in both the float observations and the GCM and emphasize how biases in ocean stratification affect model replication of ocean heat flux and sea ice melt on short timescales.

2. Methods and Data

2.1. Observations

To investigate the response of the ocean to the cyclone in observations, we make use of Argo (Wong et al., 2020) float readings (float ID #6903705) that are available from the marginal sea ice zone in the region of the Barents Sea that was most affected by the cyclone (see Figure 1a). This float provides full-depth temperature and salinity profiles at approximately 2 m vertical resolution once every 5 days, and allows us to diagnose the ocean changes associated with the passage of the cyclone. We converted in situ values of temperature and salinity profiles provided by the float to conservative temperature, Θ, and absolute salinity, S_A, in accordance with TEOS-10 (IOC et al., 2010). The floats use an ice-avoidance algorithm (van Wijk et al., 2009), so during sea ice-covered conditions (such as during the cyclone) they do not fully surface, resulting in missing data at depths shallower than ∼15 m and no fixed mooring position; recorded float locations with ice-cover are interpolated from the last fixed locations. During the open water periods in 2021 and 2022, the average distance traveled by the float during the 5-day sample interval was ∼21.0 km in 2021 and ∼9.7 km in 2022. The first and last fixed locations over the 2021–2022 ice-covered season (on 2021-11-12 and 2022-07-14) were separated by a distance of ∼93.1 km in 244 days, and from fall 2021 through the end of the float's life in winter 2022, all recorded float locations were constrained within a relatively small area (see inset in Figure 1a).

For satellite retrievals of sea ice concentration (SIC), we use the NSIDC daily climate data record (Meier et al., 2013). For estimates of the atmosphere, we use the ECMWF ERA5 reanalysis (Hersbach et al., 2020). For satellite retrievals of sea ice thickness (SIT), we use ESA's Soil Mapping Observing System (SMOS) level 3 SIT product at a 12.5 km resolution (Kaleschke et al., 2012; Tian-Kunze et al., 2014) and the blended SMOS-CryoSat merged SIT Level 4 product at a 25 km resolution.

2.2. GCM Simulations

We use the NCAR CESM1-CAM5 GCM (Gent et al., 2011), with fully coupled atmosphere, sea ice, ocean, and land components, run at a nominal 1° resolution. The model uses the CICE4 sea ice (E. C. Hunke et al., 2010) and the POP2 ocean components (Danabasoglu et al., 2012), both of which are widely used across other CMIP models. To replicate the observed cyclone in CESM1-CAM5, we use the nudging module in the model, which permits nudging the model's winds to a target state (see Blanchard-Wrigglesworth, Roach, et al., 2021 for a description of the methodology). We produce four nudged simulations that branch off January 1 restart files from existing CESM1-Large ensemble (CESM1-LENS) (Kay et al., 2015) simulations from four different years (2022, 2041, 2061, and 2081), as described in Table 1. The nudged simulations share the same forcings as the parent CESM1-LENS runs we branch from, but nudge their winds north of 45°N and above the boundary layer (850 hPa) to 6-hourly January 2022 winds, as estimated by ERA5. We refer to the ensemble of these runs as CESM-Nudge, and the individual runs as CESM-Nudge2022, CESM-Nudge2041, etc. We also run an additional ensemble of simulations that are identical to the four CESM-Nudge runs, but in which the sea ice floe size is decreased from its default value of 300 m to 3 m. We refer to this ensemble as CESM-Nudge_sfloe, and we use it to evaluate the sensitivity of changes in sea ice cover to the floe size prescribed in the model. We also run two additional members that nudge winds to ERA5 winds from 1979 to 2022 with 300 and 3 m sea ice floe sizes (CESM-Nudge2022 B and CESM-Nudge2022 B_sfloe) that are only used for analysis in Figure S1 in Supporting Information S1.

2.3. One-Dimensional Model Simulations

We conduct vertical one-dimensional sea ice-ocean coupled simulations to assess the role of the upward mixing of subsurface ocean heat on sea ice loss. We use the General Ocean Turbulence Model (GOTM; Burchard & Petersen, 1999; Umlauf et al., 2005), installed together with two external submodules, CVMix and STIM. The CVMix module (Q. Li et al., 2021) extends GOTM to include a set of vertical mixing parameterizations of Langmuir turbulence via the Community Vertical Mixing Project, together with an implementation of the K-profile parameterization (KPP) (Large et al., 1994) of surface mixing (Van Roekel et al., 2018). The STIM module (https://github.com/BoldingBruggeman/stim/) incorporates a set of simplified thermodynamic ice models in GOTM. All simulations were conducted with the full GOTM + CVMix + STIM installation (though only a subset used the parameterizations added by CVMix; described below). Through the STIM module, we implemented the Winton three-layer sea ice thermodynamic model (Winton, 2000). The "out-of-the-box"

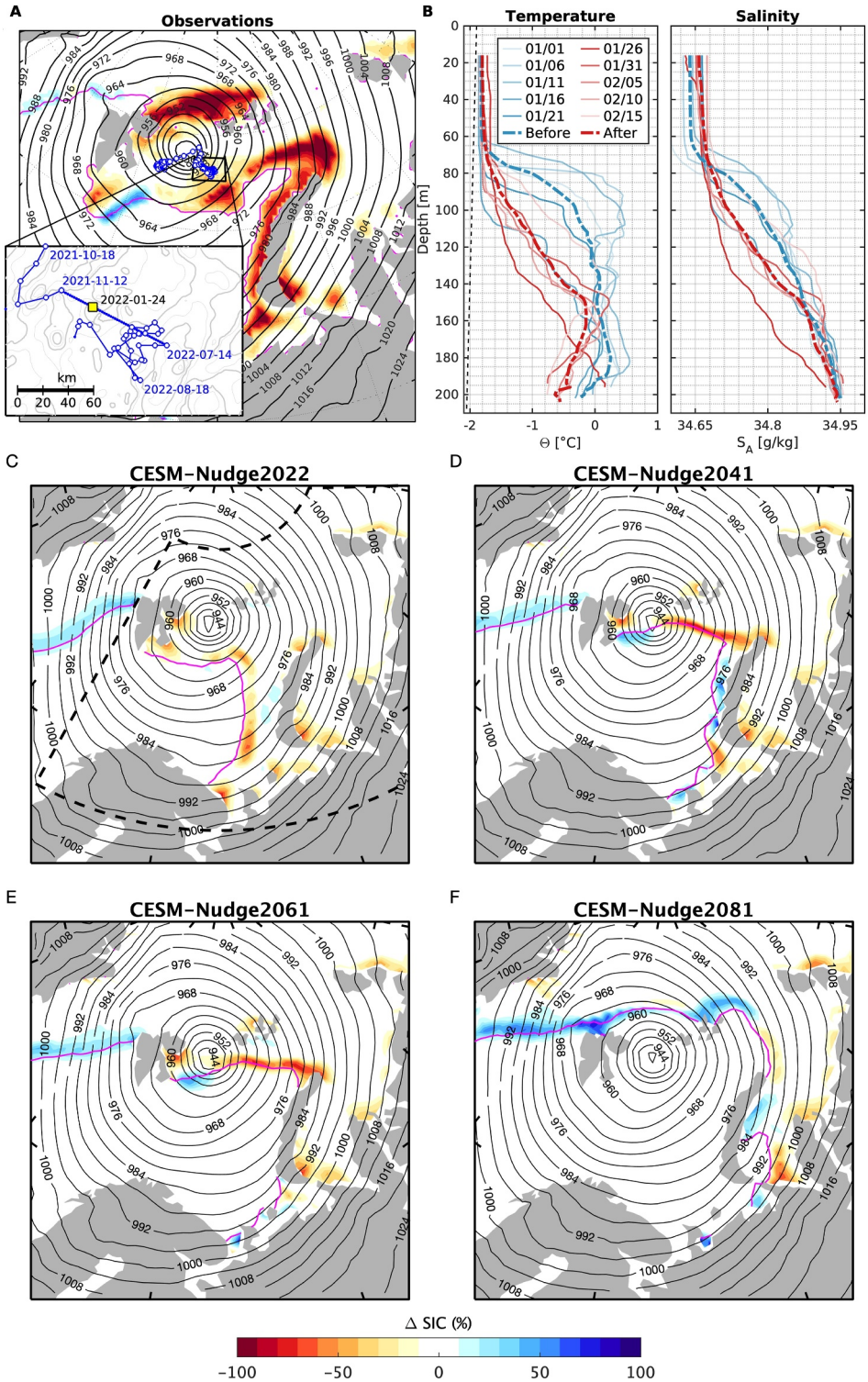

Figure 1. (a) Location of the Argo float (blue line and points), observed sea ice concentration (SIC) changes between January 21–27 (shaded), January 24 12UTC sea level pressure (black contours, labeled every 4 mb), and sea ice edge on January 24, defined as the 15% SIC contour (magenta). Open circles show when the float surfaced and reported its position; closed dots show interpolated positions. (b) Argo profiles of temperature and salinity before (in blue) and after (in red) the cyclone. Thin solid lines show individual profiles and thick colored dash-dotted lines show the mean profiles before and after. The black dashed line in the temperature panel shows the freezing temperature for water at the depth and salinity. (c–f) As in A, but for CESM-Nudge. The black dashed contour in panel (c) shows the area over which sea ice area is calculated for the Barents/Kara/West Laptev seas.

Table 1
Summary of CESM Model Simulations

Model ID	Initial conditions (from LENS run #)	Forcing year	Vertical nudging levels (hPa)	Floe size (m)
CESM-Nudge2022	2021 (LENS#21)	2022	TOM to 850	300
CESM-Nudge2041	2041 (LENS#21)	2041	TOM to 850	300
CESM-Nudge2061	2061 (LENS#21)	2061	TOM to 850	300
CESM-Nudge2081	2081 (LENS#21)	2081	TOM to 850	300
CESM-Nudge2041_sfloe	2041 (LENS#21)	2041	TOM to 850	3
CESM-Nudge2061_sfloe	2061 (LENS#21)	2061	TOM to 850	3
CESM-Nudge2081_sfloe	2081 (LENS#21)	2081	TOM to 850	3
CESM-Nudge2022 B	2022 (nudged to ERA5 1979–2022)	2022	TOM to 850	300
CESM-Nudge2022 B_sfloe	2022 (nudged to ERA5 1979–2022)	2022	TOM to 850	3

Note. In all simulations, $\alpha_{(U,V)}$ is applied over 45°N–90°N.

configuration of GOTM + STIM does not include two-way coupling between the water column and the sea ice; that is, basal heat flux from the ocean to the ice is imposed rather than calculated from upper ocean properties. To account for these effects, we adjusted the STIM module to include two-way coupling of heat and freshwater fluxes across the ice-ocean interface (see Text S1 in Supporting Information S1).

The GOTM simulations were used to assess (a) the importance of surface waves in driving mixing, and (b) whether differences in the ocean stratification between the observations and the CESM model impact the degree of vertical mixing and sea ice melt during the cyclone. To account for the former, the suite of model simulations we ran included six different turbulent mixing parameterizations associated with either shear-driven mixing (designated ST), or surface-wave-driven Langmuir turbulence (designated LT). To account for the latter, we initialized the model with ocean temperature and salinity profiles taken from either the observed Argo profiles or from the CESM-Nudge2022 simulation in the grid cell closest to the ARGO float location (CESM-Nudge2022 was taken as representative of all of the CESM-Nudge simulations given the similarity in their stratification). We set the initial SIT for all simulations to 0.70 m, which is roughly the mean SMOS SIT at the float location prior to the cyclone. We note that the results, including the modeled change in thickness, are insensitive to the choice of initial thickness, which we tested in a range from 0.5 to 1.0 m. To account for uncertainty associated with variability in the ocean structure preceding the cyclone (see Section 3.1), we initialized and ran the model forward using profiles from an ensemble of different start times, using the set of Argo profiles starting from the beginning of January (designated IC1–IC5), and equivalent CESM profiles. All model runs used a constant vertical resolution of 0.5 m and temporal resolution of 10 min, and results from all start times (IC1–IC5) were subset to a common period from 01/21–01/29. A range of output variables are available from GOTM, including, for example, vertical profiles of meridional and zonal velocities, turbulent fluxes of momentum, eddy diffusivity, among others; we make use of time-varying profiles of conservative temperature, absolute salinity, buoyancy frequency, along with SIT and melt rate. Altogether, these represent a total of 60 different simulations. We refer to each of the simulations as: [IC-Source]-[IC#]-[Mixing-ID]; for example,: ARGO-IC1-ST-MY. In these designations, [IC-Source] is either ARGO or CESM, [IC#] identifies to the different start times (IC1–IC5 correspond to start times on 01/01, 01/06, 01/11, 01/16, and 01/21, respectively), and [Mixing-ID] identifies the vertical mixing scheme used, as described in Table 2 (which represent a subset of the schemes used in Johnson et al. (2023)).

In all cases, the one-dimensional model is forced by surface stress from ERA5 reanalysis interpolated to the location of the Argo float. The reported surface stress from ERA5 reflects the net momentum flux out of the atmosphere. In sea ice-covered areas, this flux is transferred to the ocean via the sea ice, and some momentum may be lost to internal stresses within the ice (e.g., Brenner et al., 2021; Brenner, Thomson, et al., 2023). Thus, in some one-dimensional modeling applications, the momentum flux to the ocean has been estimated as a fixed fraction of the surface atmospheric stress (e.g., 33% in Wilson et al., 2019). However, sea ice break-up by waves reduces the sea ice mechanical strength (Boutin et al., 2021), which would permit greater stress transfer to the ocean. Additionally, ice breakup by waves and changing ice concentrations impact the surface roughness, an

Table 2
Summary of Turbulent Mixing Parameterizations Used for GOTM Simulations

Mixing-ID	Vertical mixing scheme	Mixing type	References
ST-MY	Mellor-Yamada (MY)	Shear (ST)	Mellor and Yamada (1982)
ST-KEPS	$k-\epsilon$	ST	Rodi (1987)
ST-CVMIX	KPP	ST	Large et al. (1994), Van Roekel et al. (2018)
LT-CVMIX-RWH16	KPP	Langmuir (LT)	Reichl et al. (2016)
LT-CVMIX-LWF16	KPP	LT	Q. Li et al. (2016)
LT-CVMIX-LF17	KPP	LT	Q. Li et al. (2017)

effect accounted for in ERA5 through atmospheric drag coefficients that vary as a function of SIC. Using the full ERA5 surface stress represents a case with ice in "free drift", with no internal stress within the sea ice and thus an upper bound on the transfer of momentum from the atmosphere to the ocean.

For simulations that include Langmuir turbulence, we estimate wave properties at the float location based on a bulk spectral attenuation scheme, using incident waves impinging on the ice edge from ERA5 (see Text S2 in Supporting Information S1, and Figures S10–S11 in Supporting Information S1). At the time of the cyclone, this estimate gives the peak significant wave height as ∼0.8 m and the peak period as ∼15.7 s, which are consistent with ICESat-2 observations. These wave estimates do not include effects of local wind wave growth (e.g., Cooper et al., 2022).

3. Results

3.1. Observed Ocean Changes

Figure 1a shows the sea level pressure (SLP) on 24 January 2022, the change in SIC between January 21 and January 27, and the location of the Argo profiles used. Throughout the full two-year lifetime of the float, it remained within a relatively constrained area in the northern Barents Sea, and the interpolated position during the January 2022 event places it near the location of maximum wind speed on January 24. Figure 1b shows the profiles of conservative temperature and absolute salinity before and after the cyclone over the full depth of the ocean (∼200 m in this area of the Barents Sea). Prior to the cyclone, there was some variability in the ARGO temperature/salinity structure (blue profiles in Figure 1b). These profiles show a nearly homogeneous surface mixed layer with a temperature close to the in situ freezing point (−1.8°C), and salinity ranging from 34.60 to 34.66 g/kg. In each case, the mixed layer was separated from warmer, more saline water at depth by a relatively sharp pycnocline. Below the pycnocline, the profiles increased to maximum subsurface temperatures of ∼0–0.5°C, and became progressively saltier, reaching a maximum salinity of ∼34.95 g/kg at depth. While broadly similar, there was moderate variability across these profiles, with mixed layer depths ranging from ∼74–106 m (defined by a $\Delta\sigma > 0.03$ kg/m^3 criteria; e.g., (Jackson et al., 2012),). The variability between profiles does not reflect a clear evolution of the ocean structure over the month leading up to the cyclone (e.g., the changing mixed layer depths were non-monotonic), and is likely due to a combination of temporal and spatial heterogeneity.

After the cyclone, there was a notable shift in the ocean structure (red profiles in 1B). Temperature profiles following the cyclone show a significant cooling below the mixed layer in a broad transition layer extending to depths of at least 150 m (and up to the full profile depth) and an erosion of the sharp pycnocline. Additionally, a salinity increase in the mixed layer and a corresponding decrease below indicate salinity mixing. In the profile on 01/26 (immediately following the cyclone), the mixed layer temperature remained elevated slightly above freezing (−1.68°C), and there was a shallow meltwater layer extending to ∼30 m visible in the salinity profile.

The change in ARGO profile characteristics before versus after the storm indicates that the ocean was significantly affected by the passage of the cyclone, and may have lost significant heat (evidenced by its cooling) to the ice/atmosphere during this event. The difference in the heat content of the mean profiles before and after the storm shows a loss of 317 MJ/m^2 — equivalent to ∼1.07 m of sea ice melt (assuming the sea ice is already at the melting point and all of the heat goes into the ice). The heat content change calculated only from the 01/21 to 01/26 profiles is equivalent to ∼0.92 m of sea ice melt This value is more than enough to account for the amount of sea

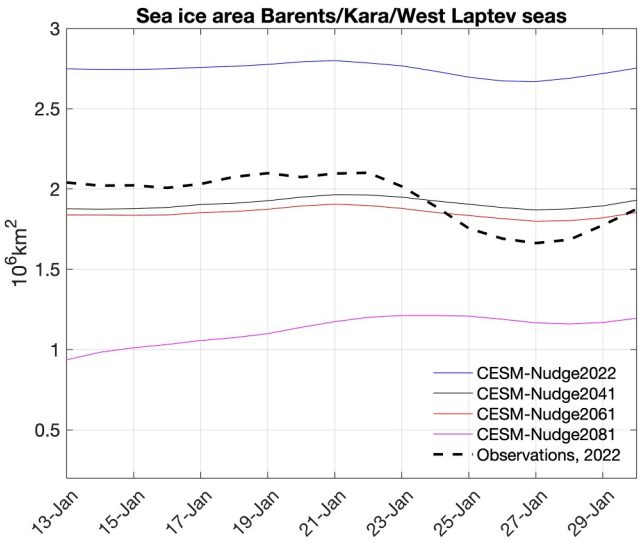

Figure 2. Daily sea ice area (SIA) between January 13 and January 30 in the Barents-Kara-West Laptev seas in CESM-Nudge and observations. SIA is summed over the area shown in the black dashed contour in Figure 1c.

ice melt that was estimated during the cyclone, when large areas of sea ice were estimated to melt by 0.25–1 m (Blanchard-Wrigglesworth et al., 2022).

3.2. Sea Ice-Ocean Changes in CESM-Nudge

In Figures 1c–1f, we show SLP and the changes in SIC between January 21 and January 27 in the CESM-Nudge simulations. Across all four simulations, SLP mirrors the observed pattern, with a deep cyclone replicated as expected given the wind-nudging methodology. The lowest SLP of the cyclone simulated in CESM-Nudge simulations is slightly higher (938 mb) than the ERA5 value (932 mb), although we note that part of this bias may be due to the lower resolution of the atmospheric model in CESM1 (about 1°lat-lon) compared to ERA5 (0.25°lat-lon). Despite only nudging the winds, surface air temperature anomalies in CESM-Nudge2022 during the cyclone are close to ERA5 anomalies (Figure S1 in Supporting Information S1).

In terms of SIC changes associated with the cyclone, in CESM-Nudge2022, CESM-Nudge2041, and CESM-Nudge2061, SIC decreases along the sea ice edge in the Barents Sea, and increases slightly in the East Greenland Sea to the west of the cyclone center. In CESM-Nudge2081, the pattern of SIC change is slightly different, with small reductions in SIC along the Kara Sea coastlines, but smaller changes or even an increase along the Barents Sea sea-ice edge, which in 2081 is located further north and east toward the central Arctic basin compared to the earlier CESM-Nudge runs.

Compared to observations (Figure 1a), it is clear that despite skillfully replicating the observed cyclone, the changes in SIC in the model are much smaller than the observed changes, and the simulated SIC loss is more limited to the sea ice edge in the Barents. The large loss of sea ice observed between northern Svalbard and the Franz Josef archipelago and the decline in SIC in most of the Kara Sea between Novaya Zemlya and the Russian mainland coastline are absent in the simulations. In addition, the simulations (especially CESM-Nudge2081) tend to overestimate the sea ice gain west of the cyclone in the East Greenland Sea.

The model biases in SIC change are reflected in the evolution of SIA over the Barents-Kara-West Laptev seas in the CESM-Nudge simulations, which we show together with observations in Figure 2. In CESM-Nudge2022,2041 and 2061, SIA drops by 0.1–0.15 million km^2 between January 21 and January 27, significantly smaller than the observed change of about 0.42 million km^2. In CESM-Nudge2081, the changes in SIA are even smaller and slightly delayed, with SIA dropping by less than 0.1 million km^2 between January 23 and January 27. In Figure S2 in Supporting Information S1, we show the same metrics for the CESM-Nudge_sfloe simulations. Overall, the results in these simulations are not significantly different from CESM-Nudge, meaning that the floe size value used in the model does not significantly impact sea ice loss in this case study, likely due to the small amount of lateral ice melt increase. Because simulated effects of floe size are weak, these runs are not discussed further.

In Figure 3, we show the changes in SIT (SIT, in m) between January 21 and January 27 in CESM-Nudge and in observations. In CESM-Nudge2021, 2041, and 2061, SIT decreases by 0.2–0.4 m along the Barents sea ice edge, whereas SIT increases in the East Greenland Sea. Changes in SIT further away from the sea ice edge in the Barents, Kara, and Laptev seas are relatively small, with some areas of SIT increase along the Severnaya Zemlya archipelago. In contrast, in observations, SIT decreased significantly (0.4–1 m) over large areas of the Barents, Kara and west Laptev seas, with a comparable SIT thinning at the ARGO float location (Figure S3 in Supporting Information S1). Changes in SIT decrease across the four individual CESM-Nudge simulations (with SIT changes in CESM-Nudge2022 being greatest and changes in CESM-Nudge2081 being smallest), despite expectations that the influence of Arctic cyclones on sea ice will increase in the future (e.g., Clancy et al., 2022).

In Figure 4 and Figure S4 in Supporting Information S1 we show the changes in SIC and SIT in CESM-Nudge2022 partitioned into their dynamic and thermodynamic tendency components, and the sum of both tendency components (we show the equivalent to Figure 4 for the remaining CESM-Nudge simulations in Figures S5–S7 in Supporting Information S1). The dynamic changes in SIC (Figure 4a) drive SIC loss along the Barents

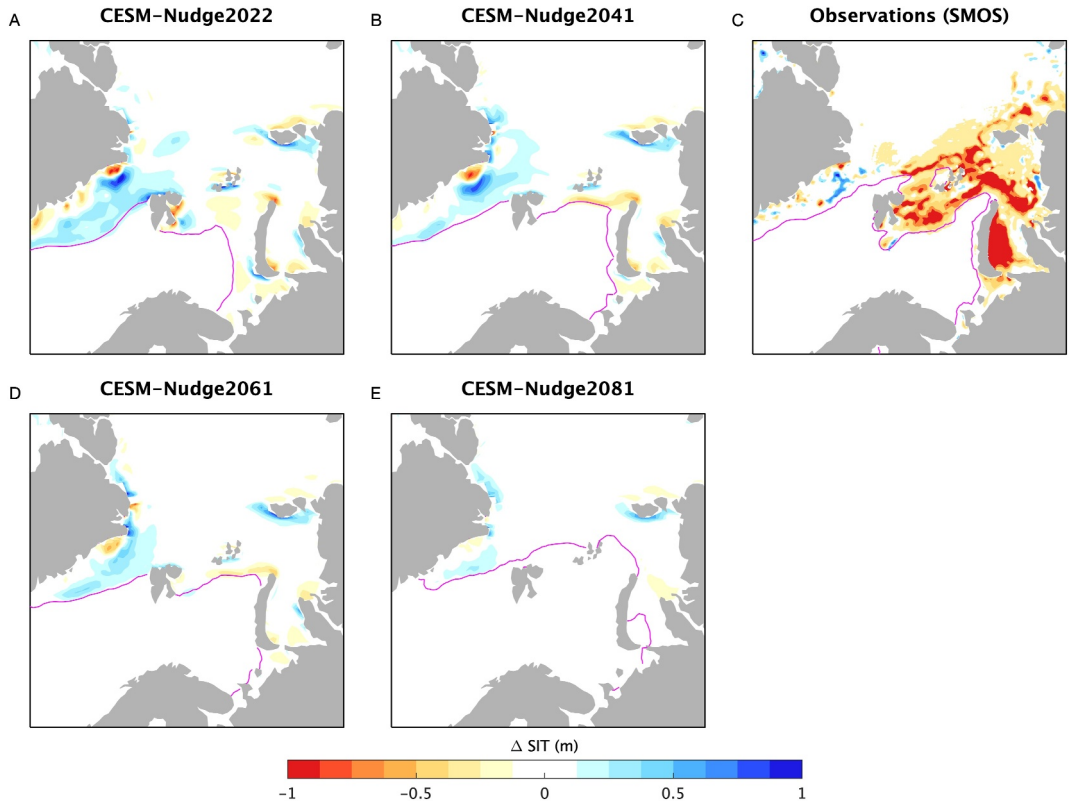

Figure 3. Change in sea ice thickness (SIT, m) from 21 to 27 January in CESM-Nudge simulations (left and middle columns) and observations (top right panel). The sea ice edge on January 24, defined as the 15% sea ice concentration contour, is shown by the magenta contour.

sea ice edge and the Barents, Kara, and west Laptev seas, and SIC gain along the East Greenland sea ice edge. In contrast, the thermodynamic SIC changes act to counteract the dynamic SIC changes (Figure 4b). The total SIC change reconstructed from the dynamic and thermodynamic tendencies (Figure 4c) shows a similar spatial footprint to the dynamic changes, albeit of lower magnitude, due to the impact of the thermodynamic tendencies, indicating that dynamics drive the total changes in SIC, which are damped by thermodynamics. Dynamic changes in SIT (Figure 4d) in the Barents/Kara/Laptev seas can drive both SIT gain and loss, with gain in regions of ice convergence (such as the western coastlines of Franz Josef and Severnaya Zemlya archipelagos), and loss in regions of ice divergence (e.g., the eastern coastlines). The thermodynamic SIT changes (Figure 4e) are much smaller, and the total SIT tendency (Figure 4f) is mostly driven by the dynamics.

Focusing on the region of largest simulated sea ice loss along the Barents sea ice edge in Figure S4 in Supporting Information S1 shows that most of the loss in sea ice is dynamic, illustrating that wind-driven sea ice motion is causing the sea ice edge to retreat in CESM-Nudge. We also investigate sea ice melt partitioned into its top melt and bottom melt components in Figure S8 in Supporting Information S1. In CESM-Nudge, any sea ice melt is taking place as bottom melt, while top melt is near-zero (including in the warmer CESM-Nudge2081 simulation). This result is consistent with ERA5 estimates, which show net energy fluxes from the surface to the atmosphere (satellite derived estimates showed a small net flux from the atmosphere to the surface, enough to melt 5 cm of sea ice over the cyclone's lifetime, Blanchard-Wrigglesworth et al., 2022).

In Figure 5, we show the model's ocean temperature and salinity profiles averaged over the region of sea ice loss in the Barents Sea in the CESM-Nudge2022 case before (21 January) and after (27 January) the cyclone (the other CESM-Nudge case studies show similar results and are not shown for simplicity). These profiles show a strong stratification, with ocean temperatures at the freezing point at depths of 0–70 m, increasing to 2°C at depths of 130–250 m. Salinity increases from 34.1 g/kg at depths of 0–70 m to 34.9 g/kg at depths of 130–250 m. Unlike in

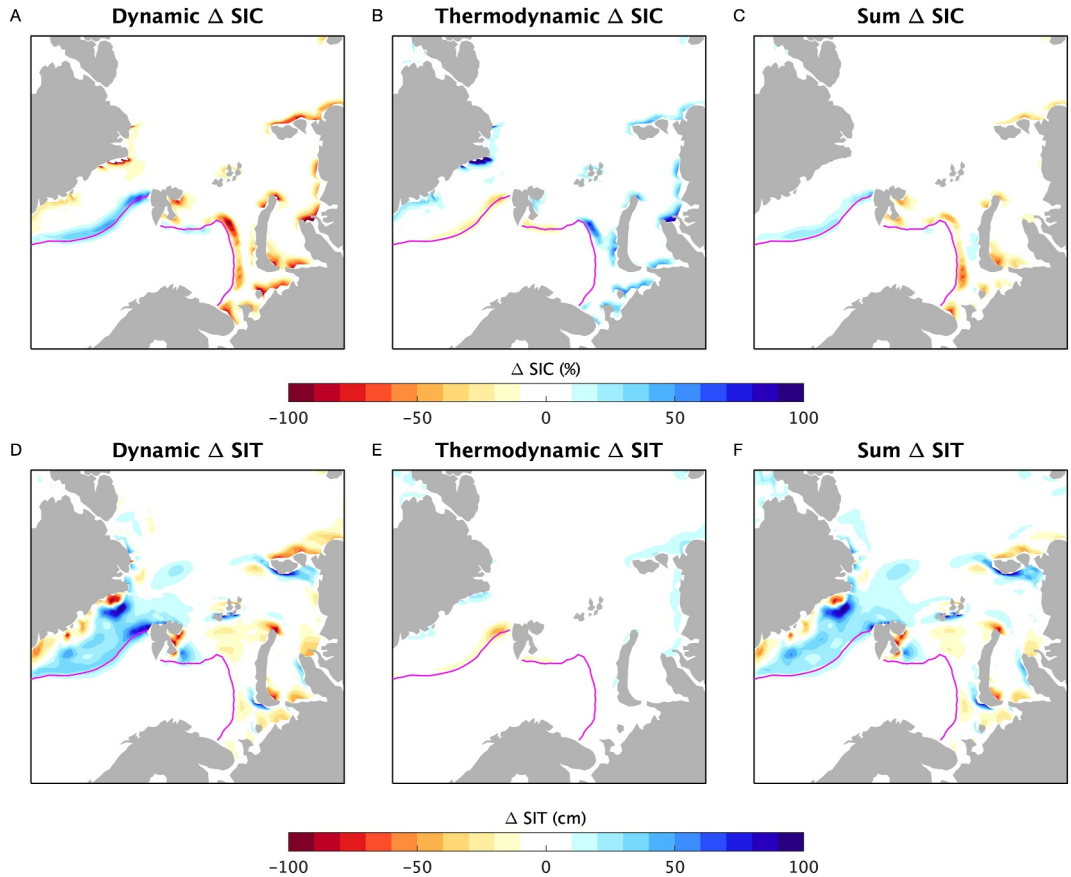

Figure 4. Changes in sea ice concentration (top row) and sea ice thickness (bottom row) between January 21 and 27 in CESM-Nudge2022, reconstructed from the dynamic (a and d) and thermodynamic tendency terms (b and e). The sum of both terms is shown in the right column (c and f).

the Argo profiles shown in Figure 1, there are very small changes in the model's temperature and salinity profiles associated with the passage of the cyclone.

A comparison of the surface stress magnitude timeseries from ERA5 and the atmosphere-ice and ice-ocean stress in CESM-Nudge2022 simulation is shown in Figure 6. While nudging winds above the boundary layer in CESM-Nudge successfully reproduced the SLP field (and thus SLP gradient force) and several ERA5 surface variables, the Figure shows that biases in the surface (atmosphere-ice) stress remained. CESM-Nudge struggles to simulate some of the very high surface stresses near the cyclone and in the warm front region (between Franz Josef and Novaya Zemlya, Figures 6a and 6b), possibly due to boundary layer physics/surface biases, and nudging to 6-hourly ERA5 winds (observations show the peak winds lasting a few hours). In particular at the location of the Argo float, in observations the surface stress bias was strongest at the time of the cyclone: during the peak stresses on 01/24, the surface stress in ERA5 was roughly 54% higher than CESM-Nudge2022 simulations (1.50 N/m2 vs. 1.00 N/m2, Figure 6a). However, averaged over January 22–26, the biases are smaller, with CESM-Nudge2022 mean atmosphere-ice stress (0.36 N/m2) being 15% lower than the ERA5-derived surface mean stress (0.41 N/m2, see Figure 6c).

3.3. Simplified Ice-Ocean Model Results

Results from the one-dimensional model emphasize the differences in vertical mixing between simulations initialized with the observed and CESM-Nudge ocean profiles. Figure 7 shows an example case of the application of the one-dimensional model from the ST-CVMIX simulation initialized with the Argo (Figure 7a) and CESM-Nudge2021 profiles (Figure 7b). When initialized with an observed Argo profile, the cyclone produces a

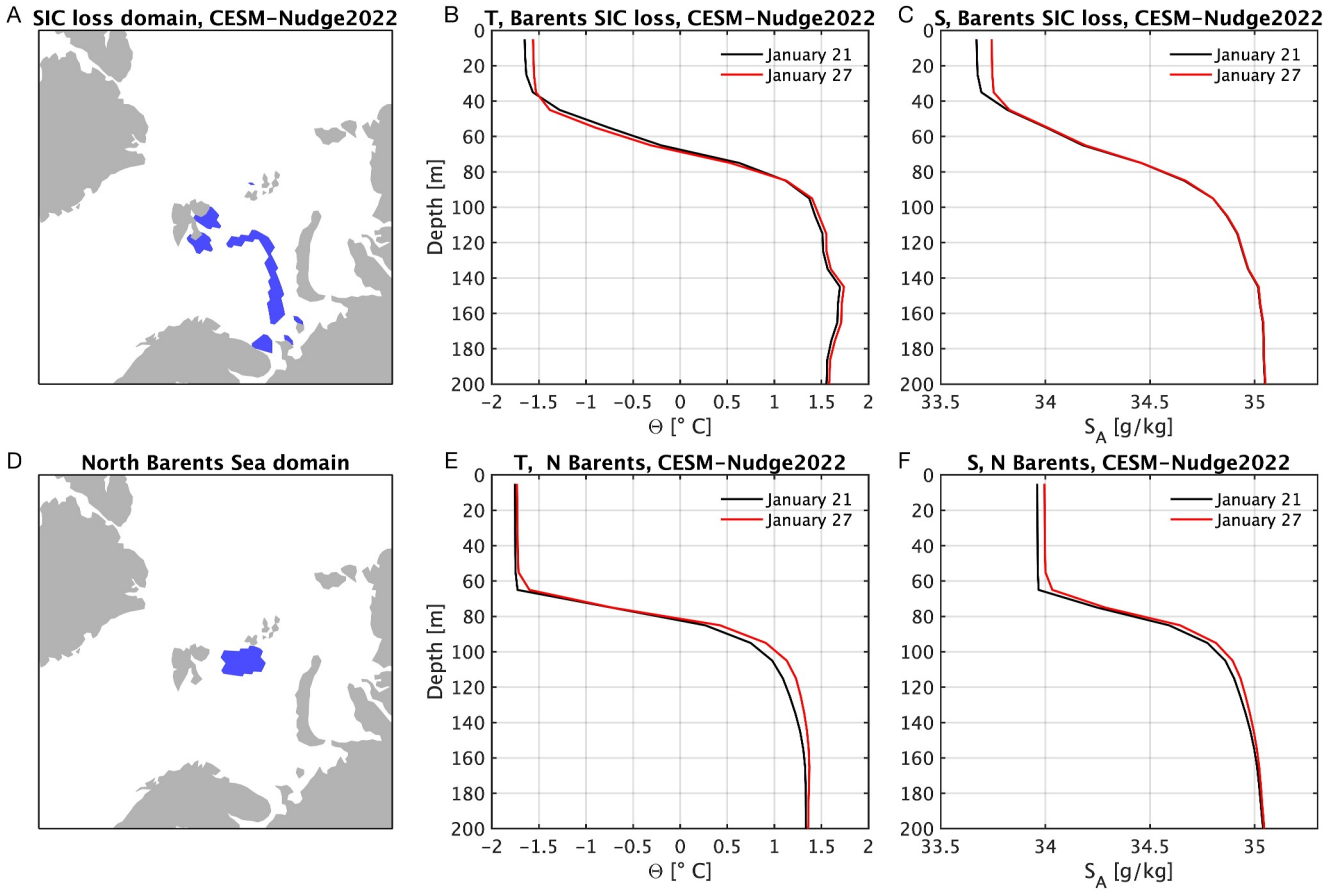

Figure 5. Profiles of temperature (b and e) and salinity (c and f) before (black) and after (red) the January 2022 cyclone averaged over the Barents sea ice loss region in CESM-Nudge2022 (top row) and in the north Barents sea (bottom row). The two domains over which T and S are averaged are shown in blue in panels (a and d).

deepening of the mixed layer, with an upward mixing of ocean heat and associated sea ice melt during the passage of the cyclone. In this example, the modeled shear-driven mixing extends to a depth of ∼120 m. In contrast, the model application to the CESM-Nudge profile shows no notable vertical mixing, and a minimal peak in ice melt rate (Figure 7b). While Figure 7 shows results from ST-CVMIX as an example, these results are qualitatively the same for all the mixing schemes tested (Figure 8 and Figure S9 in Supporting Information S1). However, details of the water column structure after mixing — and therefore the amount of heat released from the subsurface — was somewhat sensitive to the mixing parameterization scheme and the starting times of profiles used.

Figure 8 shows the final profiles at the end of the simulation for both Argo-derived (panels A–C) and CESM-Nudge derived (D–F) initial conditions. For each of the mixing parameterizations tested, the profiles shown are a median of the final profiles from the ensemble of different start times (IC1–IC5). For initial conditions from Argo profiles, all of the parameterizations produced mixing to a depth of approximately 120 m, though the width of the pycnocline varied between schemes. ST-MY and ST-KEPS schemes produced similar profiles, with a broad pycnocline, while the KPP-based schemes (ST-CVMIX and all LT schemes) had sharper, deeper pycnoclines and thus released more heat to the ice. Freshwater input from sea ice melt leads to relatively cold, fresh meltwater layers in the upper part of each profile for all schemes, with the depth of the meltwater layer extending to ∼40 m for all schemes. LT mixing schemes, which explicitly account for the effects of waves, did not differ notably from the ST-CVMIX scheme. Results from LT-CVMIX-LWF16 and LT-CVMIX-LF17 were not discernible from ST-CVMIX, while LT-CVMIX-RWH16 had only minor differences. The negligible differences between LT schemes and ST-CVMIX are likely due to the relatively small waves (peak significant wave height of ∼0.8 m) and weak Stokes drift at this distance into the ice (see Figure S10 in Supporting Information S1).

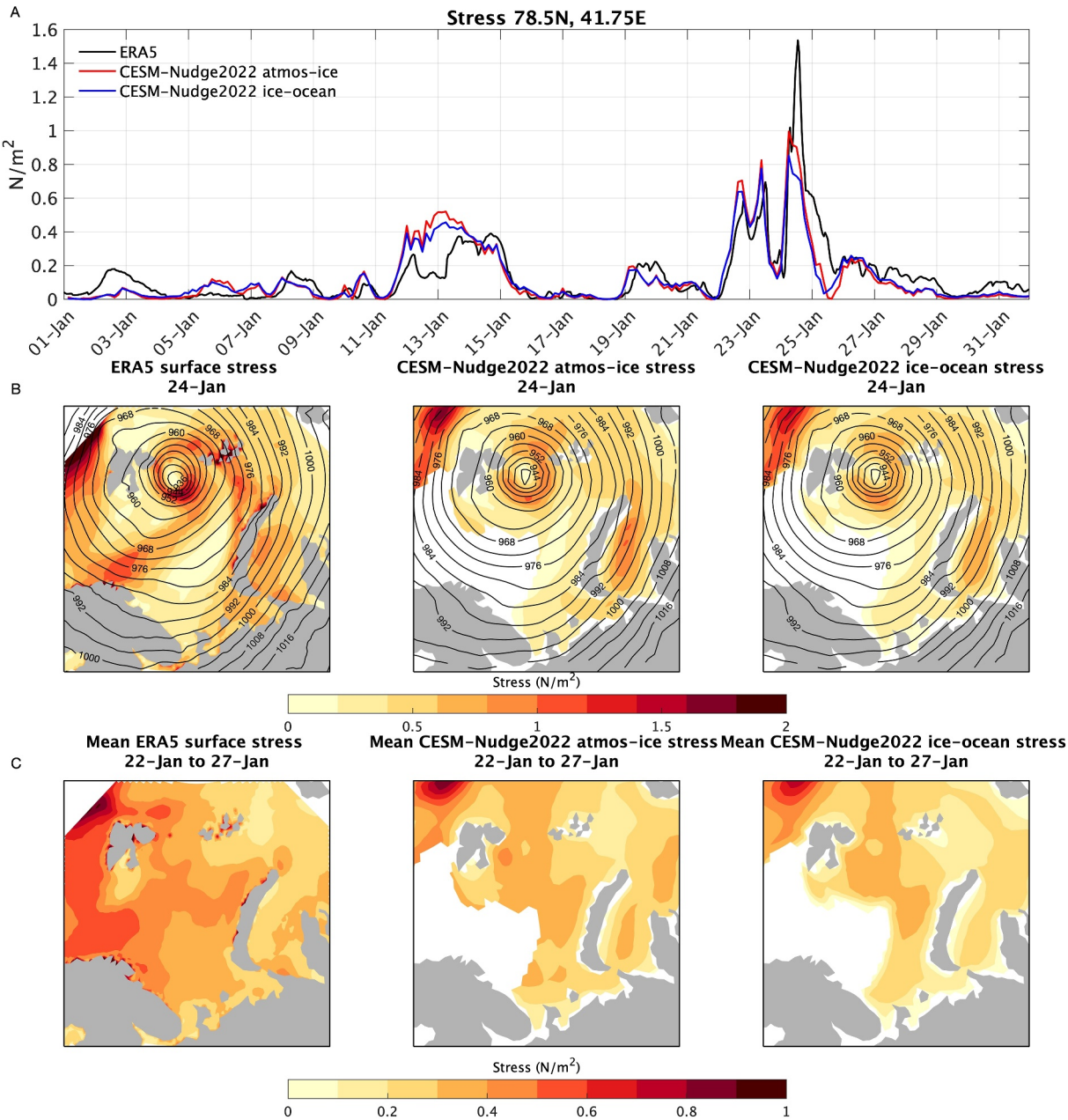

Figure 6. (a) Timeseries of surface stress magnitude at the location of the Argo float in ERA5 (black) and of atmosphere-to-ice (red) and ice-to-ocean (blue) stresses in CESM-Nudge2022, (b) spatial fields on 24 January 12 UTC of the surface stress in ERA5, and atmosphere-to-ice and ice-to-ocean stresses in CESM-Nudge2022, and (c) the time-mean fields of the same stress variables shown in panel (b) averaged over January 22–26. Note that in the CESM-Nudge2022 panels in panels (b and c), the fields have no data over open ocean regions (as there is no sea ice, shaded white).

As in the example case (Figure 7), the model initialized from CESM-Nudge profiles had minimal vertical mixing across all schemes and start times (Figures 8d–8f). Due to the lack of appreciable vertical mixing, there was little difference between the results from different mixing schemes. The small differences between schemes were similar to when the model was run with Argo profiles: ST-MY and ST-KEPS resulted in smoother transition layers, while CVMIX schemes had sharper final pycnoclines. Even in the most extreme case, mixing only extended to ~75 m.

Figure 8g shows the net sea ice melt from the GOTM simulations, compared to the observed thickness change estimated from SMOS at the float location over the same period. The median net ice melt across all ARGO runs

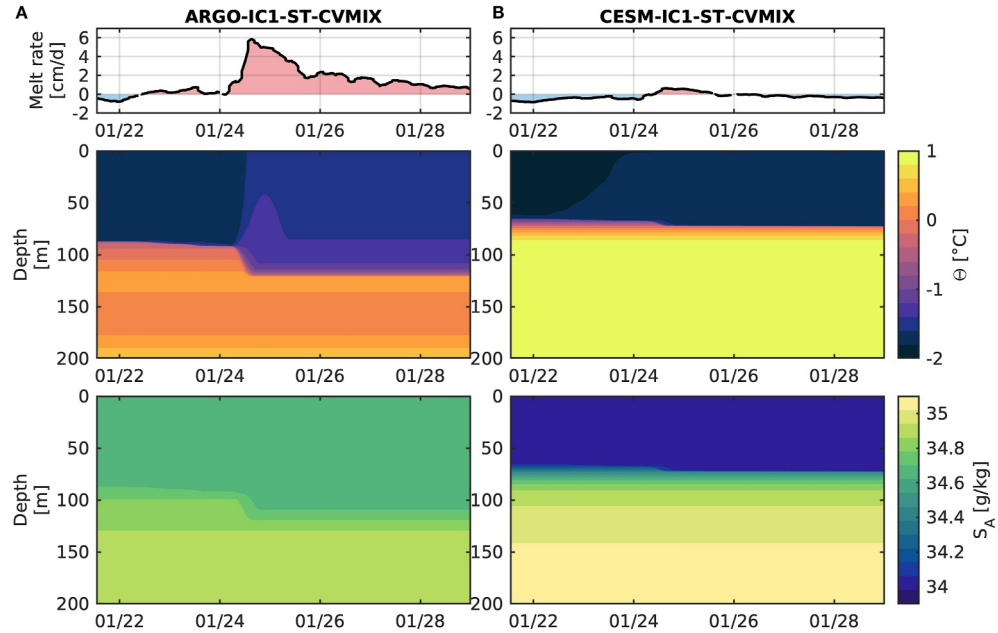

Figure 7. Timeseries of GOTM model results using the ST-CVMIX mixing parameterization for panel (a) ARGO and (b) CESM simulations, showing the evolution of sea ice melt rate (top row), ocean temperature (middle row), and ocean salinity (bottom row).

(including all start times and mixing schemes) was 0.104 m, with the medians for each mixing scheme ranging from 0.055 to 0.122 m — accounting for 11%–25% of the SMOS SIT change of 0.499 m, though within the wide observational uncertainty range (0.06–0.938 m). For simulations initialized with the CESM-Nudge profiles, the overall median had virtually no change in ice thickness (−0.003 m; i.e., ice growth), with the median for each mixing scheme ranging from −0.021 to 0.001 m. A two-sample Kolmogorov-Smirnov test ($\alpha = 0.05$) showed that the distributions of net ice melt for all Argo-derived simulations were statistically distinct from those initialized with CESM-Nudge profiles ($p = 1.1 \times 10^{-8}$).

In simulations with Argo-derived initial conditions, profiles at the end of the simulation show temperatures in the upper layer remain elevated above the freezing temperature (surface temperature range from −1.70°C to −1.57°C). As the one-dimensional model does not include ice concentration, ocean heat can only go into changing the SIT, and the ocean-ice heat flux rate is limited by the strength of the boundary layer turbulence (see Text S1 in Supporting Information S1). In reality, this residual surface layer heat would be available for further ice loss through lateral melt processes, and some heat would be released to the lower atmosphere.

3.4. Impacts of Ocean Stratification Bias in CESM

The water column structure in the CESM-Nudge simulations is markedly different than in observations (cf., Figure 1b with Figures 5 and 8d–8c with Figures 8a–8f). While both the observations and CESM feature cold, fresh surface mixed layers overlying warmer, saltier water, the simulations exhibit significantly broader salinity ranges. Specifically, surface waters in the CESM-Nudge simulations are fresher by approximately 0.6 g/kg, and deeper waters are saltier by about 0.2 g/kg. This discrepancy in salinity, which sets the water density in this temperature range, results in a model bias toward higher stratification — nearly 10 times higher peak N^2 — and enhanced water column stability, impeding mixing during the cyclone. These barriers to mixing are realized in both the CESM-Nudge simulations and the one-dimensional model simulations initialized with those profiles, with both showing minimal change in ocean structure during the cyclone.

We quantify the impact of these ocean structure differences between Argo observations and CESM-Nudge simulations by comparing the gravitational potential energy change, ΔP_g associated with mixing (e.g., Pollard et al., 1973; Reichl et al., 2022) for each of the initial conditions: $\Delta P_g = \int(\rho_m - \rho_i)gzdz$, where g is gravitational acceleration, z is the vertical coordinate, ρ_i is the density profile of the initial state, and ρ_m is the density profile of

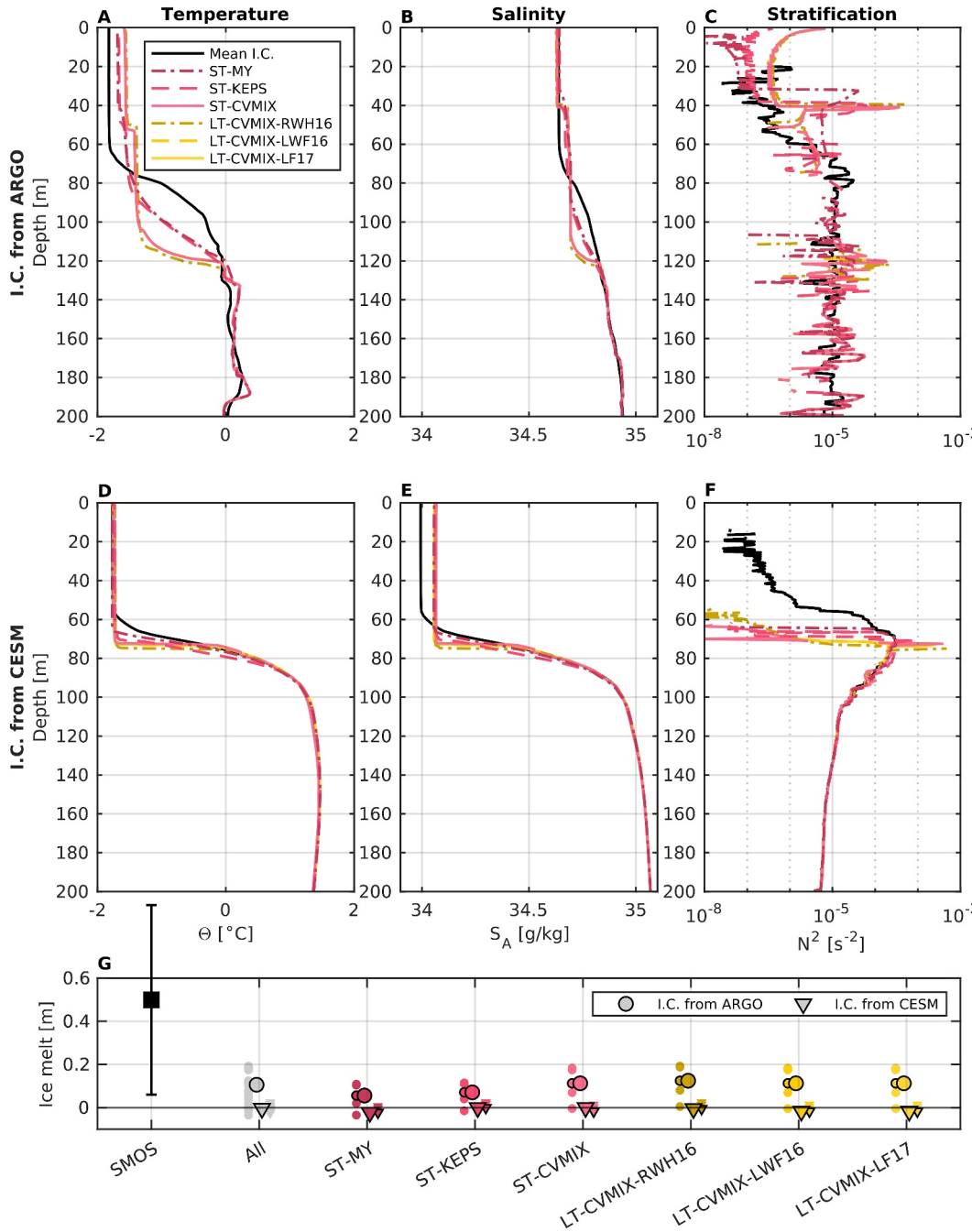

Figure 8. (a–f) GOTM simulation final profiles (median of IC1–IC5) of temperature (left column), salinity (middle column), and Stratification, N^2 (right column) for the different mixing schemes, as labeled. The first row shows simulations initialized by Argo profiles; the second row shows simulations initialized by CESM-Nudge2022 profiles. Mean IC1–IC5 profiles are shown in black for reference. (g) Net sea ice melt from Soil Mapping Observing System at the location of the float, and in the GOTM simulations, showing a compilation of all simulations (labeled "All") and for each different mixing scheme. Circular points correspond to Argo-initialized simulations and triangles are CESM-initialized. For both, small points show the results from all IC1–IC5 start times (IC5 points identified by black borders), and large points are the median results across all start times.

the mixed state (found by homogenizing temperature and salinity from the initial state within a layer of depth z_{mix}). ΔP_g represents the energy input required to mix to a depth of z_{mix}. Figure 9a shows ΔP_g as a function of mixing depth, z_{mix}, for the range of Argo-derived and CESM-derived initial profiles used in the one-dimensional

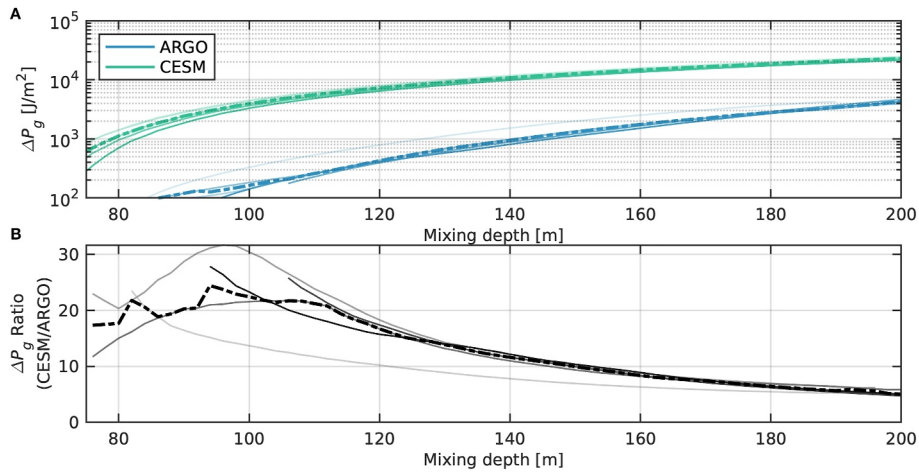

Figure 9. (a) Change in gravitational potential energy (ΔP_g) associated with mixing to a given depth for Argo profiles (blue) and CESM profiles (green). (b) The ratio of ΔP_g for CESM/ARGO profiles. Thin, solid lines in both panels correspond to all individual start times (IC1–IC5); thick dashed lines show the medians of those start times.

model tests, while Figure 9b shows the ratio of ΔP_g values calculated for the CESM profiles to the Argo profiles. As seen in the Figure, ΔP_g below the mixed layer for the CESM initial profiles was ~5–32 times higher than ΔP_g for the equivalent Argo initial profiles.

A bulk scaling approximation gives the kinetic energy input from the wind into the ocean as u_*^3 (e.g., Reichl et al., 2022), where the friction velocity u^*, is related to the surface stress as $\tau = \rho u_*^2$. Thus, achieving the same depth of mixing with the CESM water column structure would require approximately 3–10 times higher surface stress compared to observed profiles, values that are about an order of magnitude larger than the surface stress biases in CESM-Nudge shown above.

ERA5 surface stress represents an approximate upper bound on stress input to the ocean, associated with ice in free-drift (see Section 2.3). Even with dynamic redistribution of the ice in CESM (Figure 4), the loss of momentum to internal ice stresses was relatively low: the ice-ocean stress generally remained between 80% and 100% of the atmosphere-ice stress throughout the simulation, as shown in Figure 6. The inclusion of variable ice drag coefficients to account for form drag effects (e.g., Tsamados et al., 2014) might improve the representation of surface stress characteristics in CESM, but given the lack of mixing in the GOTM simulations forced by ERA5 stresses and the high potential energy barrier associated with the stratification bias, this would still likely be insufficient to overcome the stratification in the model.

In essence, the high stratification biases in CESM-Nudge dominate surface stress biases, and prevent any vertical wind-driven mixing in the model's ocean, and thus there is no source of ocean heat for thermodynamic sea ice melt.

4. Discussion and Conclusions

The record Arctic cyclone of January 2022 caused a record weekly loss of Arctic sea ice that was poorly forecast and could not be accounted for by energy fluxes from the atmosphere to the surface (Blanchard-Wrigglesworth et al., 2022). To further understand this extreme event of atmosphere/sea ice coupling, we have explored ocean characteristics from the marginal ice zone with Argo float data. These data show that the ocean column cooled significantly during the cyclone and the changes in the vertical salinity profile point to turbulent mixing that reached through the full depth of the water column. It is thus likely that the ocean played a significant role in the observed sea ice loss via upward heat fluxes and enhanced bottom melt of sea ice.

To further understand models' ability to simulate the observed sea ice loss, we have tested the skill of a widely used and validated GCM, NCAR's CESM1-CAM5. We have done this by nudging the model's winds to the observed January 2022 winds. We also test the sensitivity of changes in sea ice to sea-ice mean state by conducting four different simulations with different forcings, representative of present-day and future forcings in the

CESM1-CMIP5 forcing context, and we also test the sensitivity of sea ice changes to the floe size prescribed in the sea ice model component.

We find that, as designed, the model skillfully replicates the January 2022 cyclone. However, the simulated changes in sea ice are much smaller than observed, with simulated SIA loss of about 20% of the observed sea ice loss. The sea ice loss in the model is mostly driven by a wind-driven dynamic sea ice edge retreat. Changes in SIT are small and limited to the sea ice edge or near coastlines. Thermodynamic sea ice loss is largely insignificant. The response of sea ice to the cyclone is not sensitive to floe size. In addition, the vertical temperature and salinity structure of the ocean in the Barents Sea region is not significantly affected by the cyclone in the model simulations, with the model showing a strong stratification and well-defined mixed layer.

Why did CESM-Nudge produce so little thermodynamic melt, and why did its ocean structure remain unaltered by the passage of the cyclone? The one-dimensional model experiments provide a possible explanation: when initialized with profiles taken from CESM-Nudge, vertical mixing from the storm was not enough to erode the stratification and melt sea ice. Relative to the Argo observations, CESM-Nudge profiles had much stronger stratification and a broader salinity range. Scaling arguments based on gravitational potential energy suggest that the surface stress required to mix CESM-Nudge profiles to the same depth as Argo profiles would need to be 3–10 times higher. However, CESM-Nudge simulations also had a low bias in the surface stress during the cyclone, with mean surface stress in ERA5 during the cyclone roughly 15% higher than in CESM-Nudge simulations. Together, these effects prevent the upward mixing of ocean heat in the CESM simulations.

One of the hypotheses put forward in (Blanchard-Wrigglesworth et al., 2022) was that ocean waves played a role in the observed sea ice loss by driving ocean turbulent mixing and enhancing ocean heat fluxes to the sea ice. We partly tested this idea in GOTM by considering mixing parameterizations that included surface-wave-driven Langmuir turbulence. The results of the tests show that wave-driven turbulence was insufficient to notably alter turbulent mixing, likely because of the attenuation of waves as they travel through the sea ice and the already high level of shear-driven mixing associated with the storm. We note, however, that the Langmuir schemes tested here were devised for open water conditions, while the role of Langmuir turbulence in sea ice-covered regions requires more study. Some other indirect impacts from waves — such as the breakup of ice, and associated changes in surface roughness and loss of ice mechanical strength — were accounted for implicitly through the choice of ERA5 surface stress forcing to the model (i.e., the free-drift assumption). Thus, our results show that the ocean stratification in CESM-Nudge was so strong that simulating waves may not have resulted in significantly enhanced ocean heat fluxes at the surface.

The one-dimensional model experiments aimed to illustrate how the upward mixing of subsurface ocean heat played a role in the ice loss during the January 2022 event, rather than precisely recreating the observed ice/ocean evolution. While simulations initialized with Argo profiles do show considerable vertical mixing and ice melt, mixing did not extend to the full depth seen by the Argo float following the cyclone, and simulated SIT changes were smaller than satellite-derived estimates (though within uncertainty bounds). The discrepancy suggests the importance of other oceanographic processes associated with the passage of the cyclone, beyond those captured with a one-dimensional mixing model. For example, previous observations from the region have shown elevated turbulence associated with internal waves, and evidence of upward propagating low-mode internal wave energy (Sundfjord et al., 2007). It is possible that barotropic flow driven by the surface pressure gradient associated with the cyclone interacted with the bottom topography to generate such internal waves. In addition, SLP gradients associated with synoptic weather patterns have been shown to drive the flow of warm Atlantic water into the Barents Sea from the north (Lind & Ingvaldsen, 2012; Lundesgaard et al., 2022). These effects, which are not included in the one-dimensional model, may also be poorly captured in CESM. Despite being unable to simulate the full level of observed mixing, the results from GOTM are nonetheless useful in linking ocean heat changes to sea ice loss during the January 2022 cyclone.

The biases seen here are consistent with recent results showing that GCMs overestimate the strength of stratification on the Atlantic side of the Arctic (Dörr et al., 2024); in particular, CESM1 was among the worst-performing models at simulating stratification in the Barents Sea. In contrast, in the Western Arctic, GCMs tend to have deeper, less stratified mixed layers than observations (e.g., Dörr et al., 2024; Rosenblum et al., 2021; Rosenblum et al., 2022). This study suggests that model biases in upper ocean stratification are a major impediment to representing the effect of storms on upward ocean heat transport and sea ice cover, and that improving the skill in simulating both ocean stratification and surface processes may be crucial for improving the

simulation of high-frequency sea ice variability, which CMIP climate models pervasively under-estimate (Blanchard-Wrigglesworth, Donohoe, et al., 2021). In addition, simulated long-term trends of sea ice loss and Atlantification may also be impacted by the model's bias in simulating the ability of Atlantic water to be efficiently mixed to the surface, and may be the reason why CESM1 underestimates decadal winter sea ice loss even when its circulation is nudged to observations (Roach & Blanchard-Wrigglesworth, 2022).

Data Availability Statement

NSIDC daily SIC data (Meier et al., 2013) are available at https://nsidc.org/data/g02202, SMOS SIT data are available at https://earth.esa.int/eogateway/catalog/smos-l3-sea-ice-thickness and SMOS-CryoSat blended data at https://earth.esa.int/eogateway/catalog/smos-cryosat-l4-sea-ice-thickness ERA5 data (Hersbach et al., 2020) are available at https://www.ecmwf.int/en/forecasts/dataset/ecmwf-reanalysis-v5, CESM-LENS data are available via https://www.cesm.ucar.edu/community-projects/lens/data-sets. The Argo data are available at https://argo.ucsd.edu. Output from the nudged and 1-D simulations are available at https://atmos.washington.edu/~ed/data/cyclone.

Acknowledgments
EBW acknowledges support from NASA Grants 80NSSC20K0922, 80NSSC20K0959 and ONR-DRI Grant N00014-21-1-2490. MAW acknowledges support from NASA's ICESat-2 program JPL-1699716 and NASA Grant 80NSSC20K0922. SB and CH were supported by Schmidt Futures, a philanthropic initiative that seeks to improve societal outcomes through the development of emerging science and technologies. CH was also supported by NASA Grant 80NSSC20K0959. CMB was supported by ONR-DRI Grant N00014-21-1-2490. This work uses ERA5 data, which contains modified Copernicus Climate Change Service information 2020. Neither the European Commission nor ECMWF is responsible for any use that may be made of the Copernicus information or data it contains. The Argo data were collected and made freely available by the International Argo Program and the national programs that contribute to it (https://argo.ucsd.edu, https://www.ocean-ops.org). The Argo Program is part of the Global Ocean Observing System. We would also like to acknowledge high-performance computing support from Cheyenne (10.5065/D6RX99HX) provided by NCAR's Computational and Information Systems Laboratory, sponsored by the National Science Foundation. We also thank David Clemens-Sewall, Leah Johnson, and Zhihua Zheng for insightful discussions.

References

Allende, S., Fichefet, T., Goosse, H., & Treguier, A. (2023). On the ability of omip models to simulate the ocean mixed layer depth and its seasonal cycle in the arctic ocean. *Ocean Modelling*, *184*, 102226. https://doi.org/10.1016/j.ocemod.2023.102226

Årthun, M., Eldevik, T., Smedsrud, L. H., Skagseth, Ø., & Ingvaldsen, R. B. (2012). Quantifying the influence of Atlantic heat on Barents Sea ice variability and retreat. *Journal of Climate*, *25*(13), 4736–4743. https://doi.org/10.1175/jcli-d-11-00466.1

Asplin, M. G., Galley, R., Barber, D. G., & Prinsenberg, S. (2012). Fracture of summer perennial sea ice by ocean swell as a result of Arctic storms. *Journal of Geophysical Research*, *117*(C6), C06025. https://doi.org/10.1029/2011jc007221

Blanchard-Wrigglesworth, E., Donohoe, A., Roach, L. A., DuVivier, A., & Bitz, C. M. (2021). High-frequency sea ice variability in observations and models. *Geophysical Research Letters*, *48*(14), e2020GL092356. https://doi.org/10.1029/2020gl092356

Blanchard-Wrigglesworth, E., Roach, L. A., Donohoe, A., & Ding, Q. (2021). Impact of winds and Southern Ocean SSTs on Antarctic sea ice trends and variability. *Journal of Climate*, *34*(3), 949–965. https://doi.org/10.1175/jcli-d-20-0386.1

Blanchard-Wrigglesworth, E., Webster, M., Boisvert, L., Parker, C., & Horvat, C. (2022). Record Arctic cyclone of January 2022: Characteristics, impacts, and predictability. *Journal of Geophysical Research: Atmospheres*, *127*(21), e2022JD037161. https://doi.org/10.1029/2022jd037161

Boutin, G., Williams, T., Rampal, P., Olason, E., & Lique, C. (2021). Wave–sea-ice interactions in a brittle rheological framework. *The Cryosphere*, *15*(1), 431–457. https://doi.org/10.5194/tc-15-431-2021

Brenner, S., Rainville, L., Thomson, J., Cole, S., & Lee, C. (2021). Comparing observations and parameterizations of ice-ocean drag through an annual cycle across the Beaufort Sea. *Journal of Geophysical Research: Oceans*, *126*(4), 29. https://doi.org/10.1029/2020JC016977

Brenner, S., Thomson, J., Rainville, L., Crews, L., & Lee, C. M. (2023a). Wind-driven motions of the ocean surface mixed layer in the Western Arctic. *Journal of Physical Oceanography*, *53*(7), 1787–1804. https://doi.org/10.1175/JPO-D-22-0112.1

Burchard, H., & Petersen, O. (1999). Models of turbulence in the marine environment—A comparative study of two-equation turbulence models. *Journal of Marine Systems*, *21*(1–4), 29–53. https://doi.org/10.1016/s0924-7963(99)00004-4

Clancy, R., Bitz, C. M., Blanchard-Wrigglesworth, E., McGraw, M. C., & Cavallo, S. M. (2022). A cyclone-centered perspective on the drivers of asymmetric patterns in the atmosphere and sea ice during Arctic cyclones. *Journal of Climate*, *35*(1), 73–89.

Cooper, V. T., Roach, L. A., Thomson, J., Brenner, S. D., Smith, M. M., Meylan, M. H., & Bitz, C. M. (2022). Wind waves in sea ice of the western Arctic and a global coupled wave-ice model. *Philosophical Transactions of the Royal Society A*, *380*(2235), 19. https://doi.org/10.1098/rsta.2021.0258

Danabasoglu, G., Bates, S. C., Briegleb, B. P., Jayne, S. R., Jochum, M., Large, W. G., et al. (2012). The CCSM4 ocean component. *Journal of Climate*, *25*(5), 1361–1389. https://doi.org/10.1175/jcli-d-11-00091.1

Dörr, J., Årthun, M., Eldevik, T., & Sandø, A. B. (2024). Expanding influence of Atlantic and Pacific Ocean Heat transport on winter seasea-ice variability in a warming arctic. *Journal of Geophysical Research: Oceans*, *129*(2), e2023JC019900. https://doi.org/10.1029/2023JC019900

Gent, P., Danabasoglu, G., Donner, L., Holland, M., Hunke, E., Jayne, S., et al. (2011). The community climate System model version 4. *Journal of Climate*, *24*(19), 4973–4991. https://doi.org/10.1175/2011jcli4083.1

Gerland, S., Ingvaldsen, R. B., Reigstad, M., Sundfjord, A., Bogstad, B., Chierici, M., et al. (2023). Still Arctic? The changing Barents Sea. *Elementa: Science of the Anthropocene*, *11*(1). https://doi.org/10.1525/elementa.2022.00088

Graham, R. M., Itkin, P., Meyer, A., Sundfjord, A., Spreen, G., Smedsrud, L. H., et al. (2019). Winter storms accelerate the demise of sea ice in the atlantic sector of the arctic ocean. *Scientific Reports*, *9*(1), 9222. https://doi.org/10.1038/s41598-019-45574-5

Hersbach, H., Bell, B., Berrisford, P., Hirahara, S., Horányi, A., Muñoz-Sabater, J., et al. (2020). The ERA5 global reanalysis [Dataset]. *Quarterly Journal of the Royal Meteorological Society*, *146*(730), 1999–2049. https://doi.org/10.1002/qj.3803

Hunke, E., Allard, R., Blain, P., Blockley, E., Feltham, D., Fichefet, T., et al. (2020). Should sea-ice modeling tools designed for climate research be used for short-term forecasting? *Current Climate Change Reports*, *6*(4), 121–136. https://doi.org/10.1007/s40641-020-00162-y

Hunke, E. C., Lipscomb, W. H., Turner, A. K., Jeffery, N., & Elliott, S. (2010). *CICE: The Los Alamos sea ice model documentation and software user's manual version 4.1 la-cc-06-012. T-3 Fluid dynamics group* (Vol. 675, p. 500). Los Alamos National Laboratory.

Ilıcak, M., Drange, H., Wang, Q., Gerdes, R., Aksenov, Y., Bailey, D., et al. (2016). An assessment of the Arctic Ocean in a suite of interannual CORE-II simulations. Part III: Hydrography and fluxes. *Ocean Modelling*, *100*, 141–161. https://doi.org/10.1016/j.ocemod.2016.02.004

IOC, SCOR, & IAPSO. (2010). *The international thermodynamic equation of seawater – 2010: Calculation and use of thermodynamic properties (Tech. Rep. Nos. Intergovernmental Oceanographic Commission, Manuals and Guides No. 56)*. UNESCO.

Itkin, P., Spreen, G., Cheng, B., Doble, M., Girard-Ardhuin, F., Haapala, J., et al. (2017). Thin ice and storms: Sea ice deformation from buoy arrays deployed during n-ice 2015. *Journal of Geophysical Research: Oceans*, *122*(6), 4661–4674. https://doi.org/10.1002/2016jc012403

Jackson, J. M., Williams, W. J., & Carmack, E. C. (2012). Winter sea-Ice melt in the Canada Basin, Arctic Ocean. *Geophysical Research Letters*, *39*(3). https://doi.org/10.1029/2011GL050219

Johnson, L., Fox-Kemper, B., Li, Q., Pham, H. T., & Sarkar, S. (2023). A finite-time ensemble method for mixed layer model comparison. *Journal of Physical Oceanography*, *1*(aop), 2211–2230. https://doi.org/10.1175/JPO-D-22-0107.1

Kaleschke, L., Tian-Kunze, X., Maaß, N., Mäkynen, M., & Drusch, M. (2012). Sea ice thickness retrieval from SMOS brightness temperatures during the Arctic freeze-up period [Dataset]. *Geophysical Research Letters*, *39*(5), L05501. https://doi.org/10.1029/2012gl050916

Kay, J. E., Deser, C., Phillips, A., Mai, A., Hannay, C., Strand, G., et al. (2015). The Community Earth System Model (CESM) large ensemble project: A community resource for studying climate change in the presence of internal climate variability. *Bulletin of the American Meteorological Society*, *96*(8), 1333–1349. https://doi.org/10.1175/bams-d-13-00255.1

Khosravi, N., Wang, Q., Koldunov, N., Hinrichs, C., Semmler, T., Danilov, S., & Jung, T. (2022). The arctic ocean in cmip6 models: Biases and projected changes in temperature and salinity. *Earth's Future*, *10*(2), e2021EF002282. https://doi.org/10.1029/2021ef002282

Large, W. G., McWilliams, J. C., & Doney, S. C. (1994). Oceanic vertical mixing: A review and a model with a nonlocal boundary layer parameterization. *Reviews of Geophysics*, *32*(4), 363–403. https://doi.org/10.1029/94RG01872

Li, D., Zhang, R., & Knutson, T. R. (2017a). On the discrepancy between observed and CMIP5 multi-model simulated Barents Sea winter sea ice decline. *Nature Communications*, *8*(1), 14991. https://doi.org/10.1038/ncomms14991

Li, Q., Bruggeman, J., Burchard, H., Klingbeil, K., Umlauf, L., & Bolding, K. (2021). Integrating CVMix into GOTM (v6. 0): A consistent framework for testing, comparing, and applying ocean mixing schemes. *Geoscientific Model Development*, *14*(7), 4261–4282. https://doi.org/10.5194/gmd-14-4261-2021

Li, Q., Fox-Kemper, B., Breivik, Ø., & Webb, A. (2017b). Statistical models of global Langmuir mixing. *Ocean Modelling*, *113*, 95–114. https://doi.org/10.1016/j.ocemod.2017.03.016

Li, Q., Webb, A., Fox-Kemper, B., Craig, A., Danabasoglu, G., Large, W. G., & Vertenstein, M. (2016). Langmuir mixing effects on global climate: WAVEWATCH III in CESM. *Ocean Modelling*, *103*, 145–160. https://doi.org/10.1016/j.ocemod.2015.07.020

Lind, S., & Ingvaldsen, R. B. (2012). Variability and impacts of Atlantic water entering the Barents Sea from the north. *Deep Sea Research Part I: Oceanographic Research Papers*, *62*, 70–88. https://doi.org/10.1016/j.dsr.2011.12.007

Lind, S., Ingvaldsen, R. B., & Furevik, T. (2018). Arctic warming hotspot in the northern Barents Sea linked to declining sea-ice import. *Nature Climate Change*, *8*(7), 634–639. https://doi.org/10.1038/s41558-018-0205-y

Lundesgaard, Ø., Sundfjord, A., Lind, S., Nilsen, F., & Renner, A. H. H. (2022). Import of Atlantic Water and sea ice controls the ocean environment in the northern Barents Sea. *Ocean Science*, *18*(5), 1389–1418. https://doi.org/10.5194/os-18-1389-2022

Marko, J. R. (2003). Observations and analyses of an intense waves-in-ice event in the Sea of Okhotsk. *Journal of Geophysical Research*, *108*(C9). https://doi.org/10.1029/2001jc001214

Meier, W., Fetterer, F., Savoie, M., Mallory, S., Duerr, R., & Stroeve, J. (2013). NOAA/NSIDC climate data record of passive microwave sea ice concentration, version 2 [Dataset]. *National snow and ice data center*. https://www.ncei.noaa.gov/access/metadata/landing-page/bin/iso?id=gov.noaa.ncdc:C00808;view=html

Mellor, G. L., & Yamada, T. (1982). Development of a turbulence closure model for geophysical fluid problems. *Reviews of Geophysics*, *20*(4), 851–875. https://doi.org/10.1029/RG020i004p00851

Meyer, A., Fer, I., Sundfjord, A., & Peterson, A. K. (2017). Mixing rates and vertical heat fluxes north of s valbard from a rctic winter to spring. *Journal of Geophysical Research: Oceans*, *122*(6), 4569–4586. https://doi.org/10.1002/2016jc012441

Muilwijk, M., Nummelin, A., Heuzé, C., Polyakov, I. V., Zanowski, H., & Smedsrud, L. H. (2023). Divergence in climate model projections of future arctic atlantification. *Journal of Climate*, *36*(6), 1727–1748. https://doi.org/10.1175/jcli-d-22-0349.1

Onarheim, I. H., & Årthun, M. (2017). Toward an ice-free barents sea. *Geophysical Research Letters*, *44*(16), 8387–8395. https://doi.org/10.1002/2017gl074304

Peterson, A. K., Fer, I., McPhee, M. G., & Randelhoff, A. (2017). Turbulent heat and momentum fluxes in the upper ocean under a rctic sea ice. *Journal of Geophysical Research: Oceans*, *122*(2), 1439–1456. https://doi.org/10.1002/2016jc012283

Pithan, F., Athanase, M., Dahlke, S., Sánchez-Benítez, A., Shupe, M. D., Sledd, A., et al. (2022). Nudging allows direct evaluation of coupled climate models with in-situ observations: A case study from the MOSAiC expedition. *EGUsphere*, *1–23*.

Pollard, R. T., Rhines, P. B., & Thompson, R. O. R. Y. (1973). The deepening of the wind-Mixed layer. *Geophysical Fluid Dynamics*, *4*(4), 381–404. https://doi.org/10.1080/03091927208236105

Polyakov, I. V., Pnyushkov, A. V., Alkire, M. B., Ashik, I. M., Baumann, T. M., Carmack, E. C., et al. (2017). Greater role for Atlantic inflows on seasea-ice loss in the Eurasian Basin of the Arctic Ocean. *Science*, *356*(6335), 285–291. https://doi.org/10.1126/science.aai8204

Rantanen, M., Karpechko, A. Y., Lipponen, A., Nordling, K., Hyvärinen, O., Ruosteenoja, K., et al. (2022). The Arctic has warmed nearly four times faster than the globe since 1979. *Communications Earth & Environment*, *3*(1), 168. https://doi.org/10.1038/s43247-022-00498-3

Reichl, B. G., Adcroft, A., Griffies, S. M., & Hallberg, R. (2022). A potential energy analysis of ocean surface mixed layers. *Journal of Geophysical Research: Oceans*, *127*(7), e2021JC018140. https://doi.org/10.1029/2021JC018140

Reichl, B. G., Wang, D., Hara, T., Ginis, I., & Kukulka, T. (2016). Langmuir turbulence parameterization in tropical cyclone conditions. *Journal of Physical Oceanography*, *46*(3), 863–886. https://doi.org/10.1175/JPO-D-15-0106.1

Roach, L. A., & Blanchard-Wrigglesworth, E. (2022). Observed winds crucial for september Arctic sea ice loss. *Geophysical Research Letters*, *49*(6), e2022GL097884. https://doi.org/10.1029/2022gl097884

Rodi, W. (1987). Examples of calculation methods for flow and mixing in stratified fluids. *Journal of Geophysical Research*, *92*(C5), 5305–5328. https://doi.org/10.1029/JC092iC05p05305

Rosenblum, E., Fajber, R., Stroeve, J. C., Gille, S. T., Tremblay, L. B., & Carmack, E. C. (2021). Surface salinity under transitioning ice cover in the Canada Basin: Climate model biases linked to vertical distribution of fresh water. *Geophysical Research Letters*, *48*(21), e2021GL094739. https://doi.org/10.1029/2021GL094739

Rosenblum, E., Stroeve, J., Gille, S. T., Lique, C., Fajber, R., Tremblay, L. B., et al. (2022). Freshwater input and vertical mixing in the Canada Basin's seasonal Halocline: 1975 versus 2006–12. *Journal of Physical Oceanography*, *52*(7), 1383–1396. https://doi.org/10.1175/JPO-D-21-0116.1

Smith, M., Stammerjohn, S., Persson, O., Rainville, L., Liu, G., Perrie, W., et al. (2018). Episodic reversal of autumn ice advance caused by release of ocean heat in the Beaufort Sea. *Journal of Geophysical Research: Oceans*, *123*(5), 3164–3185. https://doi.org/10.1002/2018JC013764

Stopa, J. E., Ardhuin, F., & Girard-Ardhuin, F. (2016). Wave climate in the arctic 1992-2014: Seasonality and trends. *The Cryosphere*, *10*(4), 1605–1629. https://doi.org/10.5194/tc-10-1605-2016

Sundfjord, A., Fer, I., Kasajima, Y., & Svendsen, H. (2007). Observations of turbulent mixing and hydrography in the marginal ice zone of the Barents Sea. *Journal of Geophysical Research*, *112*(C5). https://doi.org/10.1029/2006JC003524

Tian-Kunze, X., Kaleschke, L., Maaß, N., Mäkynen, M., Serra, N., Drusch, M., & Krumpen, T. (2014). SMOS-derived thin sea ice thickness: Algorithm baseline, product specifications and initial verification. *The Cryosphere*, *8*(3), 997–1018. https://doi.org/10.5194/tc-8-997-2014

Tsamados, M., Feltham, D. L., Schroeder, D., Flocco, D., Farrell, S. L., Kurtz, N., et al. (2014). Impact of variable atmospheric and oceanic form drag on simulations of Arctic sea ice. *Journal of Physical Oceanography*, *44*(5), 1329–1353. https://doi.org/10.1175/JPO-D-13-0215.1

Umlauf, L., Burchard, H., & Bolding, K. (2005). General ocean turbulence model. Source code documentation. *Baltic Sea Research Institute Warnemünde Tech. Rep*, *63*, 346.

Van Roekel, L., Adcroft, A. J., Danabasoglu, G., Griffies, S. M., Kauffman, B., Large, W., et al. (2018). The KPP boundary layer scheme for the ocean: Revisiting its formulation and benchmarking one-dimensional simulations relative to LES. *Journal of Advances in Modeling Earth Systems*, *10*(11), 2647–2685. https://doi.org/10.1029/2018MS001336

van Wijk, E. M., Riser, S., Rintoul, S. R., Speer, K., Klatt, O., Boebel, O., et al. (2009). Observing high latitudes: Extending the core Argo array. In *EPIC3OceanObs09, conference abstract book*.

Wang, Z., Walsh, J., Szymborski, S., & Peng, M. (2020). Rapid Arctic sea ice loss on the synoptic time scale and related atmospheric circulation anomalies. *Journal of Climate*, *33*(5), 1597–1617. https://doi.org/10.1175/jcli-d-19-0528.1

Waseda, T., Nose, T., Kodaira, T., Sasmal, K., & Webb, A. (2021). Climatic trends of extreme wave events caused by Arctic Cyclones in the western Arctic Ocean. *Polar Science*, *27*, 100625. https://doi.org/10.1016/j.polar.2020.100625

Wilson, E. A., Riser, S. C., Campbell, E. C., & Wong, A. P. S. (2019). Winter upper-ocean stability and ice–ocean feedbacks in the sea ice–covered southern ocean. *Journal of Physical Oceanography*, *49*(4), 1099–1117. https://doi.org/10.1175/JPO-D-18-0184.1

Winton, M. (2000). A reformulated three-layer sea ice model. *Journal of Atmospheric and Oceanic Technology*, *17*(4), 525–531. https://doi.org/10.1175/1520-0426(2000)017<0525:artlsi>2.0.co;2

Wong, A. P., Wijffels, S. E., Riser, S. C., Pouliquen, S., Hosoda, S., Roemmich, D., et al. (2020). Argo data 1999–2019: Two million temperature-salinity profiles and subsurface velocity observations from a global array of profiling floats. *Frontiers in Marine Science*, *7*, 700. https://doi.org/10.3389/fmars.2020.00700

Zhang, J., Lindsay, R., Schweiger, A., & Steele, M. (2013). The impact of an intense summer cyclone on 2012 Arctic sea ice retreat. *Geophysical Research Letters*, *40*(4), 720–726. https://doi.org/10.1002/grl.50190

References From the Supporting Information

Breivik, Ø., Bidlot, J.-R., & Janssen, P. A. E. M. (2016). A Stokes drift approximation based on the Phillips spectrum. *Ocean Modelling*, *100*, 49–56. https://doi.org/10.1016/j.ocemod.2016.01.005

Brenner, S., Horvat, C., Hall, P., Lo Piccolo, A., Fox-Kemper, B., Labbé, S., & Dansereau, V. (2023b). Scale-dependent air-sea exchange in the polar oceans: Floe-floe and floe-flow coupling in the generation of ice-ocean boundary layer turbulence. *Geophysical Research Letters*, *50*(23), e2023GL105703. https://doi.org/10.1029/2023GL105703

McPhee, M. G. (1992). Turbulent heat flux in the upper ocean under sea ice. *Journal of Geophysical Research*, *97*(C4), 5365–5379. https://doi.org/10.1029/92JC00239

Meylan, M. H., Bennetts, L. G., Mosig, J. E. M., Rogers, W. E., Doble, M. J., & Peter, M. A. (2018). Dispersion relations, power laws, and energy loss for waves in the marginal ice zone. *Journal of Geophysical Research: Oceans*, *123*(5), 3322–3335. https://doi.org/10.1002/2018JC013776